Quantum interference test of the equivalence principle on antihydrogen

P.-P. Crépin,[1,*] C. Christen,[1] R. Guérout,[1,†] V. V. Nesvizhevsky,[2] A.Yu. Voronin,[3,4] and S. Reynaud[1,‡]

[1]*Laboratoire Kastler Brossel (LKB), Sorbonne Université, CNRS, ENS-PSL Université, Collège de France, Campus Pierre et Marie Curie, 75252 Paris, France*

[2]*Institut Laue-Langevin (ILL), 71 avenue des Martyrs, 38042 Grenoble, France*

[3]*P. N. Lebedev Physical Institute, 53 Leninsky Prospect, 117924 Moscow, Russia*

[4]*Russian Quantum Center, 100 A, Novaya Street, Skolkovo, 143025 Moscow, Russia*

(Received 27 November 2018; published 22 April 2019)

We propose to use quantum interferences to improve the accuracy of the measurement of the free-fall acceleration $\bar{g}$ of antihydrogen in the gravitational behavior of antihydrogen at rest (GBAR) experiment. This method uses most antiatoms prepared in the experiment and it is simple in its principle, as interferences between gravitational quantum states are read out without transitions between them. We use a maximum likelihood method for estimating the value of $\bar{g}$ and assess the accuracy of this estimation by a Monte Carlo simulation. We find that the accuracy is improved by approximately three orders of magnitude with respect to the classical timing technique planned for the current design of the experiment.

DOI: 10.1103/PhysRevA.99.042119

I. INTRODUCTION

Gravitational properties of antimatter raise an important question in the context of the matter-antimatter asymmetry problem [1–4]. Experimental knowledge on this question is much less precise than for gravitational properties of ordinary matter [5–7]. For example, the aim of measuring the free-fall acceleration $\bar{g}$ of antihydrogen ($\overline{\mathrm{H}}$) in Earth's gravitational field has been approached only recently [8], with the sign of $\bar{g}$ not even known yet. Several collaborations are working with antihydrogen atoms produced at CERN to improve the accuracy of $\bar{g}$ measurement in dedicated experiments [9–11].

The Gravitational Behavior of Antihydrogen at Rest (GBAR) Collaboration is installing an experiment at CERN, using the techniques of ultracold atom physics to cool down antihydrogen atoms to microkelvin temperatures [12]. This makes feasible the aim of measuring $\bar{g}$ with an accuracy of the order of 1% by timing the classical free fall of antiatoms from a well-defined free-fall height [13,14]. In this paper, we propose to improve the accuracy of this measurement with the same cloud of ultracold antihydrogen atoms by using the idea of quantum techniques drawn from experiments performed by inducing transitions between gravitationally bound quantum states (GQSs) of ultracold neutrons [15–18].

Ultracold neutrons bounce above a matter surface due to the repulsive Fermi interaction [19]. For atoms, quantum bounces may be produced by the rapidly varying attractive van der Waals–Casimir-Polder interaction above the surface [20–32]. The mechanism is expected to work with antihydrogen atoms, thus preventing their annihilation at the matter surface [33–36].

Atoms with a low vertical velocity above the surface are trapped by the combined action of quantum reflection and gravity [37,38]. They can thus stay in quantum levitation states for long times which can exceed 1 s over a helium surface [39]. With the quantum interference technique studied in this paper, which is inspired by studies of neutron whispering gallery modes [40], the transition frequencies between these states are not perturbed by any mechanism inducing transitions. They are well known in the case of perfect quantum reflection and only submitted to shifts due to the Casimir-Polder interaction which have been precisely calculated [41]. It follows that the accuracy of the $\bar{g}$ measurement can be improved by using quantum interference techniques on these quantum levitation states.

II. OUTLOOK

In this article we propose a method that consists of measuring the coordinates in space and time of the annihilation of antihydrogen atoms on a detector, thus producing an interference pattern. Similar methods were used in experiments on the neutron whispering gallery [40] and we present here a detailed study of the method applied to antihydrogen atoms. In contrast to previous ideas [42], there is no need for selection of a velocity, which allows for a large gain in accuracy while effectively using most the antihydrogen atoms.

The method assumes simultaneous measurement of many gravitational quantum states, thus enormously increasing statistics compared to previous proposals [43,44] which considered one or a few quantum states. Practical implementation of this method is also simple, since it does not require precision optics and mechanics or the selection of a single quantum state.

We give below a precise description of the quantum interference technique which should lead to a largely improved accuracy for $\bar{g}$ measurement. Starting from the ultracold

*pierre-philippe.crepin@lkb.upmc.fr
†romain.guerout@lkb.upmc.fr
‡serge.reynaud@lkb.upmc.fr

 ©2019 American Physical Society

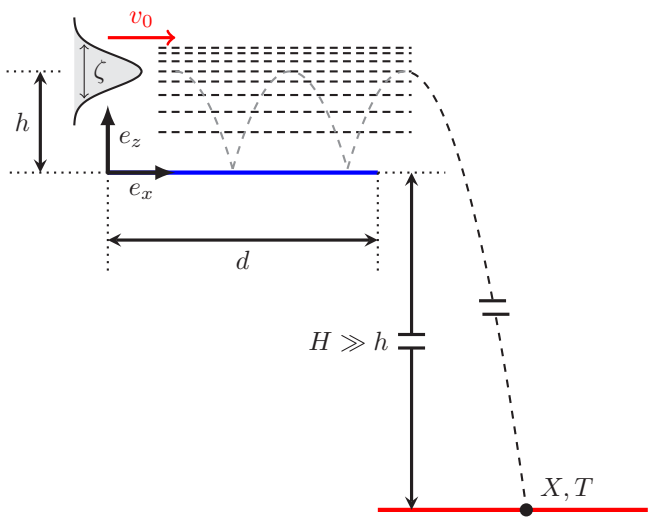

FIG. 1. Schematic of the experimental setup. The mirror, of length d, is shown as the blue horizontal line and the detector, a distance H below, as the red horizontal line. X and T are the positions in space and time of the detection events (e_x axis horizontal, e_z axis vertical). The wave packet has initially a mean height h above the mirror, a dispersion ζ, and a horizontal velocity v_0. Parabolas represent a classical motion with rebounds above the mirror, while dashed horizontal lines represent the paths through different quantum states which interfere in the detection pattern.

antihydrogen $\overline{\mathrm{H}}^+$ ions prepared in the GBAR experiment, the method appears as the sequence of steps schematized in Fig. 1.

First, the $\overline{\mathrm{H}}^+$ wave packet is prepared as the ground state of an ion trap [10,13], submitted to a kick giving it a mean horizontal velocity v_0 and irradiated with a laser photodetachment pulse which releases freely falling $\overline{\mathrm{H}}$ atoms. The kick can be produced, for example, by electrostatic means or by the photodetachment process.

Atoms then bounce above a surface, treated here as a perfect quantum reflector, and the quantum paths corresponding to different GQSs interfere. The interference pattern thus produced is detected after a macroscopic free fall down to a horizontal detection plate. Analysis of the distribution in space and time gives access to the estimation of $\overline{g}$.

This estimation is in principle sensitive to the initial distribution of the atoms after the kick, and this distribution will have to be determined from the envelope of the detection pattern, as discussed below. In the following, we choose a simple model for this distribution, which is sufficient for the purpose of the present paper.

In Fig. 1 as well as in the text, lowercase letters represent quantities relative to the first stages of preparation and interference above the mirror, while uppercase letters represent quantities associated with the free-fall and detection stages. In the following, $\overline{g}$ is simply written g and the standard value $g \simeq 9.81\ \mathrm{m\,s^{-2}}$ is used for numerical applications and plots.

III. INTERFERENCE OF GRAVITATIONAL QUANTUM STATES

Atoms of mass m are released at height h above the perfectly reflecting mirror, in a Gaussian wave packet factorized along the x and z axis $\Psi_0(x,z) = \phi_0(x)\psi_0(z)$, which minimizes the Heisenberg uncertainty relation

$$\psi_0(z) = \left(\frac{1}{2\pi\zeta^2}\right)^{1/4} \exp\left(-\frac{(z-h)^2}{4\zeta^2}\right),$$
$$\phi_0(x) = \left(\frac{1}{2\pi\zeta^2}\right)^{1/4} \exp\left(-\frac{x^2}{4\zeta^2} + i\frac{mv_0}{\hbar}x\right), \qquad (1)$$

where ζ is the dispersion of positions, identical along the 2 axis, and v_0 the velocity kick.

Here, we consider the simple model where this distribution is not modified by the kicking mechanism. As stated, this point will have to be verified in forthcoming experiments, and this can be done by analyzing the envelope of the detection pattern. The purpose of the present paper is to evaluate the accuracy which can be obtained once the initial distribution is known and our simple model is sufficient for this purpose.

The wave packet obeying the Schrödinger equation remains factorized $\Psi_t(x,z) = \phi_t(x)\psi_t(z)$ as long as the atoms remain in the quantum levitation states above the reflecting surface. This condition of separability of the Hamiltonian in x and z coordinates imposes constraints on the quality of the mirror surface roughness and material homogeneity, and the latter can be met.

The horizontal evolution leads to a mere spreading of the wave packet. The vertical evolution can be decomposed on the orthogonal basis of Airy functions,

$$\psi_t^n(z) = \Theta(z)\frac{\mathrm{Ai}(z/\ell_g - \lambda_n)}{\sqrt{\ell_g}\,\mathrm{Ai}'(-\lambda_n)} \exp(-i\lambda_n t/t_g)\,, \qquad (2)$$

where Θ is the Heaviside step function describing a perfect reflection at the surface, Ai is the first Airy function, and $(-\lambda_n)$ its nth 0; t_g, ℓ_g, and p_g are the typical time, length, and momentum scales determined by $\hbar$, m, and g, respectively:

$$t_g \equiv \left(\frac{2\hbar}{mg^2}\right)^{1/3} \simeq 1.09\ \mathrm{ms}\,,$$
$$p_g \equiv \frac{\hbar}{\ell_g} \equiv (2\hbar m^2 g)^{1/3} \simeq 1.79 \times 10^{-29}\ \mathrm{kg\,m\,s^{-1}}\,. \qquad (3)$$

The wave function $\psi_t(z)$ can be read $\sum_n c_n \psi_t^n(z)$, with the c_n's obtained by using the orthogonality properties of the ψ_t^n basis. When the vertical dispersion of ψ_t is sufficiently small compared with h, they have an analytical expression [36]:

$$c_n \simeq \frac{\zeta^{1/2}}{\ell_g^{1/2}} \frac{(8\pi)^{1/4}}{\mathrm{Ai}'(-\lambda_n)} \mathrm{Ai}\left(\frac{h}{\ell_g} - \lambda_n + \frac{\zeta^4}{\ell_g^4}\right)$$
$$\times \exp\left[\frac{\zeta^2}{\ell_g^2}\left(\frac{h}{\ell_g} - \lambda_n + \frac{2}{3}\frac{\zeta^4}{\ell_g^4}\right)\right]. \qquad (4)$$

Parameters in the initial wave packet Ψ_0, namely, the mean height h, standard deviation ζ, and velocity kick v_0, have to be chosen so as to optimize the measurement. By tuning the initial Gaussian wave packet up to reasonable values, one can indeed achieve different superposition of states. For example, choosing parameters so that the number of low-lying GQSs involved remains small leads to a simple interference pattern with a good contrast on the detector screen. On the contrary, a mixture of a large number of higher-lying GQSs leads to a

smaller contrast, because the different states present minima and maxima at different positions. We restrict the discussion of the range of parameters that can be experimentally achieved, as known from the existing analysis of the GBAR experiment [13,14].

We choose for all calculations and plots a length of the reflecting surface $d = 5$ cm and a height of free fall $H = 30$ cm, an initial height above the surface $h = 10$ μm, and a position dispersion $\zeta = 0.5$ μm. The latter value corresponds to atoms released from an harmonic trap with an oscillation frequency $\omega/(2\pi) = 20$ kHz, which is also a velocity dispersion $\simeq 6.3$ cm s^{-1} or a zero-point energy $\simeq 42$ peV ($\simeq 0.48$ μK in equivalent temperature units).

These parameters lead to a large number of interfering GQSs, which produces patterns with a high resolution and allows for a good sensitivity to the value of g, as discussed below. The final results do not depend in a critical manner on these choices, though the detailed values are in principle affected.

The high-lying QGSs are truncated by putting an absorber at some height above the quantum reflecting mirror [42]. We account for 100 GQSs, which corresponds to an absorbing mirror placed at ~ 360 μm above the mirror and leads to $\sim 20\%$ $\overline{\mathrm{H}}$ atoms lost in the absorber.

The interaction of a wave with a rough surface was studied for neutrons [45–48], and the physics is the same for the antihydrogen case. The presence of the absorber may induce a couple of extra quantum states (above the absorber height) which do not affect significantly the interference pattern, which involves many states.

Finally, the kick velocity v_0 is chosen with the prime criterion that most prepared antiatoms are used in the measurement. This requires that v_0 exceeds the standard deviation of the initial velocity distribution by a large enough factor. Another constraint is that most atoms survive their flight above the reflecting surface in a realistic situation where quantum reflection is not perfect.

Estimations in [39] have shown that the best surface for that purpose is liquid helium at a sufficiently low temperature to suppress the effect of residual vapors, on which antihydrogen in GQSs can bounce for times exceeding 1 s, which also applies for a number of bounces exceeding a few hundred. Additionally, a velocity that is too low results in a final pattern of detections concentrated around the same spot on the plate, making accurate estimation more difficult.

Several values are chosen below for the kick velocity which satisfy all of the constraints discussed above. Figures are plotted for $v_0 = 0.8$ m s^{-1} for the sake of good visibility, while Monte Carlo simulations at the end of the paper are done with an optimized $v_0 = 0.25$ m s^{-1}.

IV. READOUT OF THE INTERFERENCE PATTERN

The interference pattern produced in the interference zone above the reflecting surface is read out after a free fall from the positions in space and time of annihilation events of antihydrogen at the detector. Since the height of the free fall is much larger than the position dispersion of the wave packet above the mirror, the free fall can be considered classical (more details below). The free fall thus acts in a similar way as a diffraction process, with the *space and time positions* of the annihilation event on the detector reading the *interaction time and momentum* of the atom leaving the interference zone.

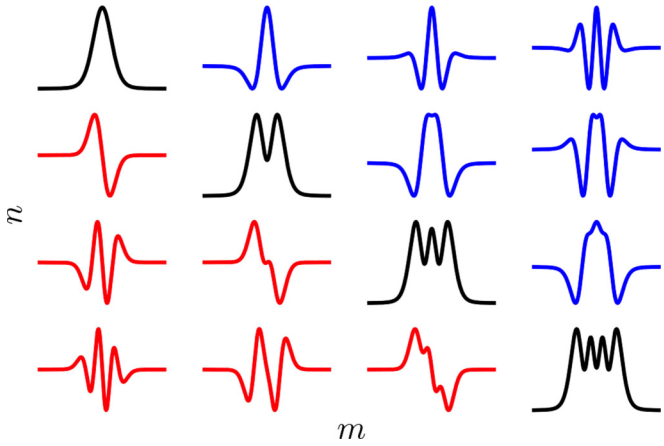

FIG. 2. Behavior of $\pi_{n,m}(p_z)$ for $1 \leqslant n, m \leqslant 4$. The diagonal cases $m = n$ are real functions, shown as black curves. The nondiagonal cases are complex functions, with their real and imaginary parts plotted, respectively, in blue above the diagonal and in red below the diagonal.

The description of quantum evolution is thus performed by two different methods in the interference zone and in the free-fall zone, with the wave function matched at the virtual surface separating the two zones. This matching corresponds to the continuity of the wave function (and its derivative) at the surface $x = d$ with $\Psi(d^-, z) = \Psi(d^+, z)$, so that we can write $\Psi(d, z)$ without creating confusion there.

This treatment amounts to neglecting diffraction at the end side of the mirror and horizontal quantum reflection induced by the change in the potential landscape at $x = d$. The same approximation used in the theoretical description of neutron whispering gallery modes leads to a satisfactory agreement with experiments [40,44].

This implies that the relevant quantity after the interference zone is the squared wave function in the momentum representation. We denote $\widetilde{\psi}_t(p_z)$ the Fourier transform of $\psi_t(z)$ and calculate the relevant signal as the probability in momentum space of the wave function: :

$$\Pi_t(p_z) = |\widetilde{\psi}_t(p_z)|^2 = \sum_{n,m} c_n c_m^* \pi_{n,m}(p_z) e^{i\omega_{nm}t} ,$$

$$\pi_{n,m}(p_z) \equiv \widetilde{\psi}_n(p_z)(\widetilde{\psi}_m(p_z))^* . \tag{5}$$

The functions $\pi_{n,m}(p_z)$ are represented in Fig. 2 for the first values of n and m. The diagonal cases $m = n$ are real-valued functions $|\widetilde{\psi}_n(p_z)|^2$, shown as black curves. The nondiagonal cases $m \neq n$ give complex functions; their real parts are plotted as blue curves above the diagonal, while their imaginary parts are plotted as red curves below the diagonal (exchanging the roles of n and m corresponds to complex conjugation).

The diagonal cases show *multibump camel* shapes corresponding to autocorrelation functions of the Fourier transform of the Airy function (n bumps for $\pi_{n,n}$). Meanwhile, the off-diagonal terms contribute as oscillations with time frequency $\omega_{nm} \equiv (\lambda_n - \lambda_m)/t_g$ in the expansion of $\Pi_t(p_z)$, with cross-correlation functions having more complex forms and

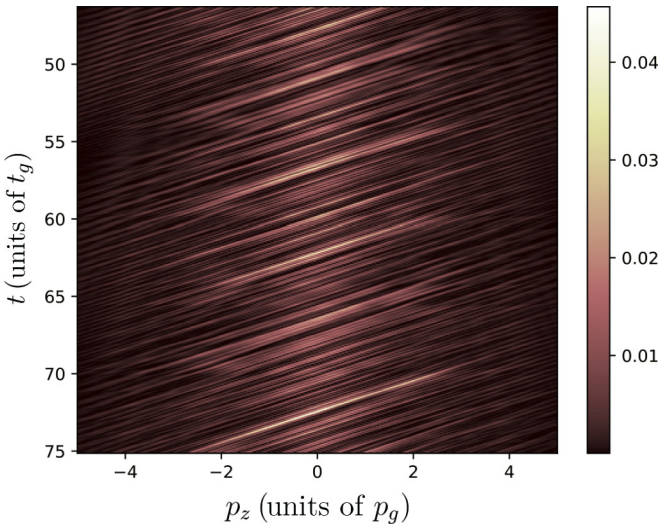

FIG. 3. Probability density in momentum space $\Pi_t(p_z)$ at the end of the interference zone for $\zeta = 0.5$ μm, $h = 10$ μm, and $v_0 = 0.8$ m s^{-1} as a function of p_z (horizontal axis, unit p_g) and t (vertical axis, unit t_g; unit chosen for the distribution so that it is normed).

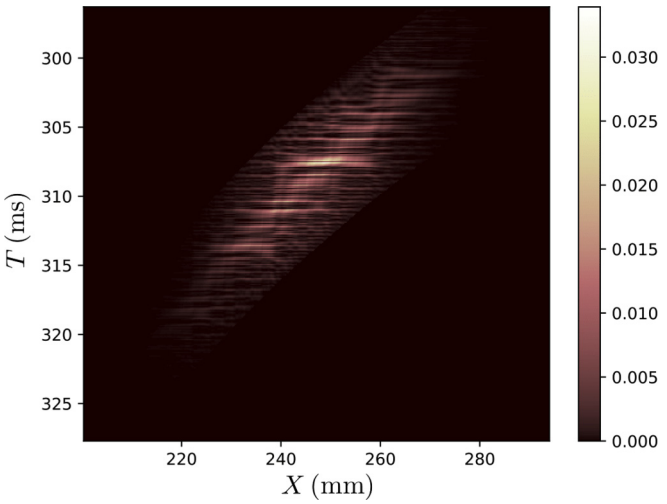

FIG. 4. Probability current density $|J(X,T)|$ on the detection plate for $\zeta = 0.5$ μm, $h = 10$ μm, and $v_0 = 0.8$ m s^{-1} as a function of X (horizontal axis; in mm) and T (vertical axis, in ms; unit chosen for the distribution so that it is normed).

non-null phases. The final detection picture discussed below reveals this complex interference pattern, which depends on the value g, allowing one to estimate g from the observed pattern.

At this stage, it is relevant to examine function (5) plotted in Fig. 3 for the values of the initial parameters discussed above. It corresponds to interference of hundreds of different GQSs, with a high weight for the lower-lying energy states. The resulting probability density in the momentum representation shows quasiperiodic oscillations with a somewhat complex shape. The abrupt transitions from a negative p_z to a symmetrically positive p_z correspond to bounces. The time bounds are chosen to delimit the portion of the signal that partakes in the observed interference pattern on the detection plate.

We now compute the current probability density $J(X,T)$ on the horizontal detection plate, where X and T are the positions in space and time of the detection event. We assume for simplicity that antiatoms are annihilated with 100% probability on the detection plate, as their kinetic energy is high after a free-fall height $H = 30$ cm. The current $J(X,T)$ is written using the Wigner function [49,50]. The free-fall evolution of this function is classical, as the potential varies linearly with z, which implies the following relations [36],

$$\begin{aligned} J(X,T) &= \int_{\mathbb{R}^2} dP_x dP_z \frac{P_z}{m} W_T(X,Z,P_x,P_z) \\ &= \int_{\mathbb{R}^2} dp_x dx P_z \frac{P_z}{m} W_t(x,z,p_x,p_z), \\ X &= x + \frac{p_x \tau}{m}, \quad Z = z + \frac{p_z \tau}{m} - \frac{g\tau^2}{2}, \\ P_x &= p_x, \quad P_z = p_z - mg\tau, \quad \tau \equiv T - t, \end{aligned} \tag{6}$$

with W_T the Wigner function at time T.

These relations can be solved for parameters t, x, z, p_x, and p_z in terms of those associated with the detection event. A second-degree equation has to be solved to extract the free-fall time τ, but the extraction may be simplified by using the fact that the free-fall height H is much larger than all typical length scales h, ζ at the end of the interference zone, and consequently, the final momentum P_z is much higher than the typical momentum at the end of the interference zone.

Using this macroscopic approximation for the free fall to the detection zone, we finally write $J(X,T)$ from the marginal of the Wigner function after the interference zone, integrated over the space variable, which is also the probability in momentum space Π:

$$\begin{aligned} |J(X,T)| &\equiv \frac{gm^2}{\overline{\tau}} |\widetilde{\phi_t}(p_x)|^2 \Pi_t(p_z)\,, \\ t &= \overline{\tau}\frac{d}{X-d}, \quad \overline{\tau} \equiv \sqrt{\frac{2H}{g}}, \\ p_x &= \frac{m(X-d)}{\overline{\tau}}, \quad p_z = mg\left(T - \frac{\overline{\tau}X}{X-d}\right)S. \end{aligned} \tag{7}$$

The probability density $|J(X,T)|$ [$J(X,T) < 0$ for freely falling atoms] is given from the probability density $\Pi_t(p_z)$ through a simple anamorphosis and weighting by the probability density of the horizontal momentum $|\widetilde{\phi_t}|^2$. The resulting $|J(X,T)|$ is plotted in Fig. 4 for the same parameters as in Fig. 3. The units are millimeters for X and milliseconds for T, with these scales showing clearly that the event detection resolution, of the order of 0.1 mm in space and 0.1 μs in time in the current GBAR design, is largely sufficient for getting the interference pattern in full detail.

In order to understand the relationship between Fig. 3 and Fig. 4, it is worthwhile to look at the anamorphosis relations when fixing T or X and observe the resulting variations of t, p_x, or p_z:

$$\begin{aligned} &\delta X = 0 \to \delta t = \delta p_x = 0, \quad \delta p_z = mg\delta T; \\ &\delta T = 0 \to \frac{\delta t}{t} = \frac{\delta p_x}{p_x} = -\frac{\delta X}{X-d}, \quad \delta p_z = -mg\,\delta t. \end{aligned} \tag{8}$$

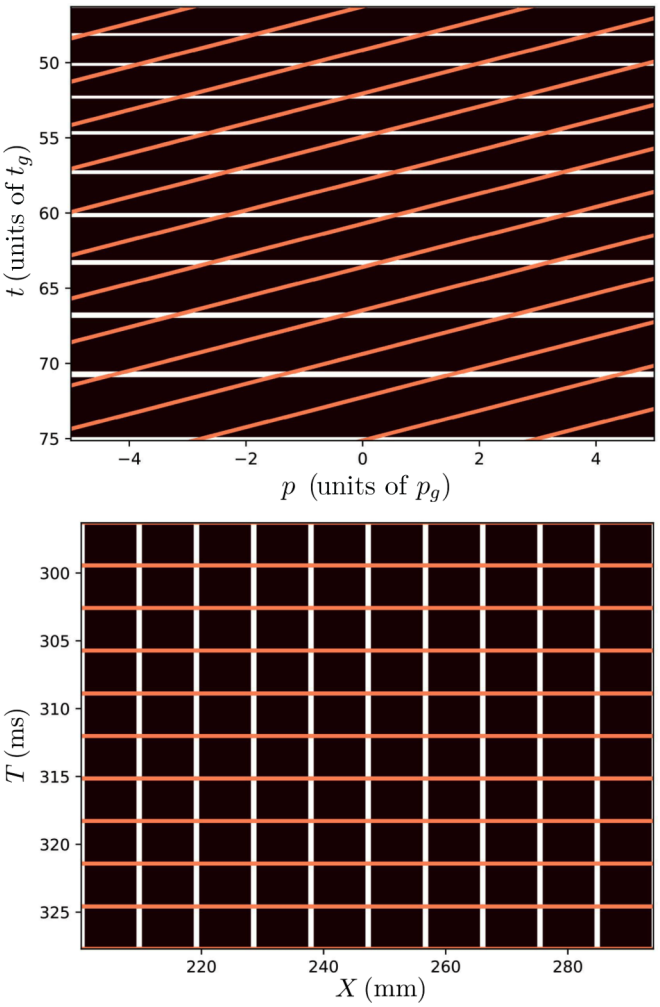

FIG. 5. Grids of lines transformed into one another by the anamorphosis at the end side of the mirror (top) and on the detection plate (bottom). Orange lines represent constructive interferences; they correspond to classical free-fall trajectories on the mirror and to horizontal lines on the detector ($\delta T = 0$). White lines are horizontal in the upper plot ($\delta t = 0$) and vertical in the lower plot ($\delta X = 0$). The bounds for the two plots are the same as in Figs. 3 and 4, respectively.

The bright oblique lines corresponding to constructive interferences and classical free-fall movements in Fig. 3 become the bright horizontal lines in Fig. 4, which correspond to constructive interferences and are parallel to the X axis on the detector plate. This discussion is illustrated by the two plots in Fig. 5, where orange lines represent constructive interferences transformed into one another by the anamorphosis. Meanwhile, white lines, also transformed into one another by the anamorphosis, are vertical on the detector ($\delta X = 0$) and horizontal in the plot corresponding to the end of the mirror ($\delta t = 0$).

We also stress at this point that the positions of X and T in the detection pattern are directly measuring the momenta along the two axes in the initial distribution. Analyzing the envelope of the detection pattern thus allows one to assess the parameters of this distribution, which would have to be done as the first step of the analysis for real experimental data. Here we subsequently consider that the initial distribution is known.

V. UNCERTAINTY ESTIMATION

We now estimate the uncertainty in the estimation of the value of g from the interference pattern registered on the detection plate. As the distance between fringes depends on g, it is tempting to measure g directly from it. This technique is, however, unpractical here, because we have only a small number of annihilation events with which to sample the details of the probability distribution. We use a much more robust maximum likelihood method to estimate the parameter g and then deduce a variance for this estimation.

We assume that we have 1000 prepared $\overline{\mathrm{H}}$ atoms, which is also $N = 800$ detection events with 20% of $\overline{\mathrm{H}}$ atoms lost in the absorber. We thus draw randomly 800 detection events in the probability distribution $\mathbb{P}_{g_0}$, corresponding to an *a priori* value of the acceleration, say the standard value g_0. We consider that this random draw of detection events $\mathcal{D} = \{(X_i, T_i),\ 1 \leqslant i \leqslant N\}$ simulates the output of one experiment.

We then use a maximum likelihood method to get an estimator $\hat{g}$ of the parameter g as would be done in the data analysis of the experiment. This estimator $\hat{g}$ maximizes the likelihood of the random draw $\mathcal{D}$ to reproduce the distributions $\mathbb{P}_g$ corresponding to different *a posteriori* values of the parameters:

$$\mathbb{L}_{\mathcal{D}}(g) = \prod_{i=1}^{N} \mathbb{P}_g(X_i, T_i),$$

$$\ln \mathbb{L}_{\mathcal{D}}(g) = \sum_{i=1}^{N} \ln \mathbb{P}_g(X_i, T_i), \tag{9}$$

$$\left(\frac{\partial \ln \mathbb{L}_{\mathcal{D}}(g)}{\partial g}\right)_{\hat{g}} = 0.$$

Figure 6 shows quadratic fits of the log likelihood functions (i.e., Gaussian fits of the likelihood functions) around their extrema. These fits correspond to 15 random draws of 800 events, with each fit yielding an estimator $\hat{g}$ of the parameter g and an estimator $\hat{\sigma}_g$ of the dispersion associated with this estimator:

$$\ln \mathbb{L}_{\mathcal{D}}(g) \approx -a_{\mathcal{D}} g^2 + b_{\mathcal{D}} g + c_{\mathcal{D}}\ ,$$

$$\hat{g} = \frac{b_{\mathcal{D}}}{2a_{\mathcal{D}}}, \quad \hat{\sigma}_g = \frac{1}{\sqrt{2a_{\mathcal{D}}}}\ . \tag{10}$$

We have normalized the Gaussians so that the variation of their variance is seen more easily as a variation of their height. The variation of the peaks shows the dispersion of the estimator $\hat{g}$ around g_0 for different random draws. The number of 15 draws has been chosen to illustrate this variance while simultaneously avoiding confusion in the figure. The variation of $\hat{g}$ and the value $\hat{\sigma}_g$ are estimators of the uncertainty in the measurement of g, which both tend to be reliable if the statistical efficiency of the method is good [51].

The statistical efficiency of the method is indeed found to be quite good, as the dispersions $\hat{\sigma}_g$ in Fig. 6 are close to the Cramer-Rao lower bound given by the Fisher information $\mathcal{I}_g$ in the detection pattern [51,52] ($\mathbb{E}$ is used to denote

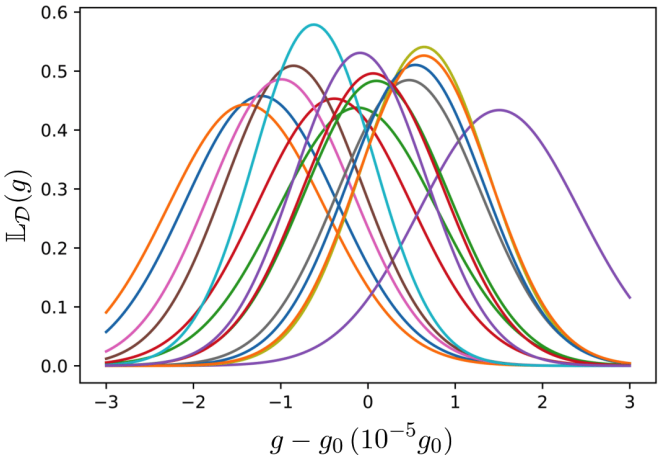

FIG. 6. Gaussian distributions obtained by a quadratic fit of the log-likelihood function calculated for 15 random draws of $N = 800$ atoms. The Gaussians are normalized so that the variation of their variance is seen more easily as a variation of their height. Colors have no meaning; they only allow one to distinguish the various functions. The horizontal axis scales as $(g - g_0)/g_0 \times 10^5$.

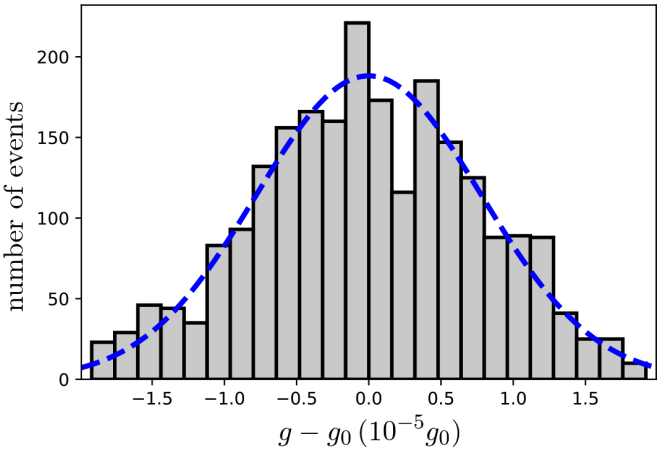

FIG. 7. Histogram of the relative variations $(\hat{g} - g_0)/g_0 \times 10^5$ obtained by repeating 2300 times a Monte Carlo simulation on 800 events, for $\zeta = 0.5$ μm, $h = 10$ μm, and $v_0 = 0.25$ m s^{-1}. The vertical axis counts the number of events per channel. The dashed blue line is a Gaussian fit of the histogram.

expectation values, Σ_g^2 is the variance of $\hat{g}$):

$$\Sigma_g^2 \geqslant \frac{1}{N\mathcal{I}(g)}\,,$$
$$\mathcal{I}(g) = \mathbb{E}\left[-\frac{\partial^2}{\partial g^2}\ln \mathbb{P}_g\right] = \mathbb{E}\left[\left(\frac{\partial}{\partial g}\ln \mathbb{P}_g\right)^2\right]. \quad (11)$$

The second expression in (11), giving the Fisher information $\mathcal{I}(g)$, explains why the precision in the estimation of g is greater for interference patterns exhibiting fine details depending on the parameter g. In simple words, these details act as thin graduations that make it easier to observe small displacements and distortions of the interference pattern when g is varied.

In order to give a robust estimation of the variance, we have finally repeated the full procedure for M different random draws of the N points. The histogram shown in Fig. 7 corresponds to $M = 2300$ such draws of the N points, with the parameters ζ and h corresponding to Fig. 4, and the velocity $v_0 = 0.25$ m s^{-1}. The dotted blue line is a Gaussian fit of the histogram which gives the dispersion Σ_g, now calculated on a large number M of experiments repeated under the same conditions:

$$\Sigma_g \simeq 7.8 \times 10^{-6} g. \quad (12)$$

The dispersion Σ_g is obtained by repeating a numerical experiment under conditions where the real experiment cannot be repeated due to the small number of available $\overline{\mathrm{H}}$ atoms. It is more reliable than the value obtained directly on a single draw corresponding to a single experiment. Thanks to the good efficiency, however, the expectation value of the estimator $\hat{\sigma}_g$ obtained in a single draw is close to it ($\mathbb{E}(\hat{\sigma}_g) \simeq 7.5 \times 10^{-6} g \simeq \Sigma_g$), while its relative dispersion is small (dispersion of $\hat{\sigma}_g/\,\mathbb{E}(\hat{\sigma}_g) \simeq 8\%$).

VI. DISCUSSION

The calculations presented in this paper show that a large improvement in g measurement accuracy may in principle be attained using quantum interference methods rather than classical timing. We now compare quantitatively the uncertainty of the quantum interference method with that of the classical timing measurement corresponding to the current design of GBAR, by using the same parameters in the quantum and classical methods. To this aim, we repeat the same discussion as in the previous section for the classical experiment, which leads to a relative uncertainty on that measurement $\Sigma_g/g = 1.7 \times 10^{-3}$.

The initial position dispersion $\zeta = 0.07$ μm considered in the current design of GBAR corresponds to a larger vertical velocity dispersion, which dominates the relative uncertainty in that measurement and it leads to the relative uncertainty $\Sigma_g/g = 1.2 \times 10^{-2}$ expected for this current design.

The spectacular improvement of Σ_g/g is due partly to the change in the initial dispersion but the more important effect is associated with the change from a classical measurement to a quantum one. The interpretation of this change is intuitively clear, as the quantum interference pattern contains much more information than the classical one, which explains why the uncertainty in the estimation of g is much better.

As discussed above, this analysis is reliable as long as the variance obtained in the Monte Carlo simulation is close to the Cramer-Rao lower bound. When the number N of atoms decreases, the distance of the two values increases, meaning that the statistical efficiency is degraded. Our simulations show that the efficiency would remain good enough if the number of available atoms was smaller than currently expected, so that the precision of the quantum method would remain by far better than that of the classical method.

A lower kick velocity would enhance the duration of the interference period above the mirror while also increasing the probability of the atom's being annihilated. For a realistic treatment of the uncertainty calculation, we should thus

describe the reflection on the surface by adding an energy-dependent annihilation probability at each bounce of the atom above the surface [41]. It would also be necessary to take into account quantum reflection on the detection plate [35].

Of course, other improvements would be required to develop a reliable data analysis of the experiment when needed, as many details have been omitted in the preliminary analysis presented in this paper. We feel that they would not change the main conclusion of this paper, namely, that the quantum interference technique opens attractive perspectives for more accurate equivalence principle tests on antihydrogen atoms.

ACKNOWLEDGMENTS

Thanks are due to P. Cladé and M.-P. Gorza for insightful discussions about uncertainty estimation and also to our colleagues in the GBAR and GRANIT collaborations.

[1] H. Bondi, Negative mass in general relativity, Rev. Mod. Phys. **29**, 423 (1957).

[2] J. Scherk, Antigravity: A crazy idea? Phys. Lett. B **88**, 265 (1979).

[3] M. M. Nieto and T. Goldman, The arguments against antigravity and the gravitational acceleration of antimatter, Phys. Rep. **205**, 221 (1991).

[4] G. Chardin and G. Manfredi, Gravity, antimatter and the Dirac-Milne universe, Hyperfine Interact. **239**, 45 (2018).

[5] E. G. Adelberger, B. R. Heckel, C. W. Stubbs, and Y. Su, Does Antimatter Fall with the Same Acceleration as Ordinary Matter? Phys. Rev. Lett. **66**, 850 (1991).

[6] T. W. Darling, F. Rossi, G. I. Opat, and G. F. Moorhead, The fall of charged particles under gravity: A study of experimental problems, Rev. Mod. Phys. **64**, 237 (1992).

[7] F. M. Huber, R. A. Lewis, E. W. Messerschmid, and G. A. Smith, Precision tests of Einstein's weak equivalence principle for antimatter, Adv. Space Res. **25**, 1245 (2000).

[8] The ALPHA Collaboration and A. E. Charman, Description and first application of a new technique to measure the gravitational mass of antihydrogen, Nat. Commun. **4**, 1785 (2013).

[9] A. Kellerbauer, M. Amoretti, A. S. Belov, G. Bonomi, I. Boscolo, R. S. Brusa, M. Büchner, V. M. Byakov, L. Cabaret, C. Canali, C. Carraro, F. Castelli, S. Cialdi, M. de Combarieu, D. Comparat, G. Consolati, N. Djourelov, M. Doser, G. Drobychev, A. Dupasquier, G. Ferrari, P. Forget, L. Formaro, A. Gervasini, M. G. Giammarchi, S. N. Gninenko, G. Gribakin, S. D. Hogan, M. Jacquey, V. Lagomarsino, G. Manuzio, S. Mariazzi, V. A. Matveev, J. O. Meier, F. Merkt, P. Nedelec, M. K. Oberthaler, P. Pari, M. Prevedelli, F. Quasso, A. Rotondi, D. Sillou, S. V. Stepanov, H. H. Stroke, G. Testera, G. M. Tino, G. Trénec, A. Vairo, J. Vigué, H. Walters, U. Warring, S. Zavatarelli, and D. S. Zvezhinskij, Proposed antimatter gravity measurement with an antihydrogen beam, Nucl. Instrum. Methods Phys. Res. Sec. B **266**, 351 (2008).

[10] P. Indelicato, G. Chardin, P. Grandemange, D. Lunney, V. Manea, A. Badertscher, P. Crivelli, A. Curioni, A. Marchionni, B. Rossi, A. Rubbia, V. Nesvizhevsky, D. Brook-Roberge, P. Comini, P. Debu, P. Dupré, L. Liszkay, B. Mansoulié, P. Pérez, J.-M. Rey, B. Reymond, N. Ruiz, Y. Sacquin, B. Vallage, F. Biraben, P. Cladé, A. Douillet, G. Dufour, S. Guellati, L. Hilico, A. Lambrecht, R. Guérout, J.-P. Karr, F. Nez, S. Reynaud, C. I. Szabo, V.-Q. Tran, J. Trapateau, A. Mohri, Y. Yamazaki, M. Charlton, S. Eriksson, N. Madsen, D. P. van der Werf, N. Kuroda, H. Torii, Y. Nagashima, F. Schmidt-Kaler, J. Walz, S. Wolf, P.-A. Hervieux, G. Manfredi, A. Voronin, P. Froelich, S. Wronka, and M. Staszczak, The GBAR project, or How does antimatter fall? Hyperfine Interact. **228**, 141 (2014).

[11] W. A. Bertsche, Prospects for comparison of matter and antimatter gravitation with ALPHA-g, Philos. Trans. R. Soc. London A **376**, 0265 (2018).

[12] J. Walz and T. W. Hänsch, A proposal to measure antimatter gravity using ultracold antihydrogen atoms, Gen. Relativ. Gravit. **36**, 561 (2004).

[13] P. Pérez, D. Banerjee, F. Biraben, D. Brook-Roberge, M. Charlton, P. Cladé, P. Comini, P. Crivelli, O. Dalkarov, P. Debu, A. Douillet, G. Dufour, P. Dupré, S. Eriksson, P. Froelich, P. Grandemange, S. Guellati, R. Guérout, J. M. Heinrich, P.-A. Hervieux, L. Hilico, A. Husson, P. Indelicato, S. Jonsell, J.-P. Karr, K. Khabarova, N. Kolachevsky, N. Kuroda, A. Lambrecht, A. M. M. Leite, L. Liszkay, D. Lunney, N. Madsen, G. Manfredi, B. Mansoulié, Y. Matsuda, A. Mohri, T. Mortensen, Y. Nagashima, V. Nesvizhevsky, F. Nez, C. Regenfus, J.-M. Rey, J.-M. Reymond, S. Reynaud, A. Rubbia, Y. Sacquin, F. Schmidt-Kaler, N. Sillitoe, M. Staszczak, C. I. Szabo-Foster, H. Torii, B. Vallage, M. Valdes, D. P. Van der Werf, A. Voronin, J. Walz, S. Wolf, S. Wronka, and Y. Yamazaki, The GBAR antimatter gravity experiment, Hyperfine Interact. **233**, 21 (2015).

[14] B. Mansoulié and on behalf of the GBAR Collaboration, Status of the GBAR experiment at CERN, Hyperfine Interact. **240**, 11 (2019).

[15] V. V. Nesvizhevsky, H. G. Börner, A. K. Petukhov, H. Abele, S. Baeßler, F. J. Rueß, T. Stöferle, A. Westphal, A. M. Gagarski, G. A. Petrov, and A. V. Strelkov, Quantum states of neutrons in the Earth's gravitational field, Nature **415**, 297 (2002).

[16] V. V. Nesvizhevsky, H. G. Börner, A. M. Gagarski, A. K. Petoukhov, G. A. Petrov, H. Abele, S. Baeßler, G. Divkovic, F. J. Rueß, Th. Stöferle, A. Westphal, A. V. Strelkov, K. V. Protasov, and A. Yu. Voronin, Measurement of quantum states of neutrons in the Earth's gravitational field, Phys. Rev. D **67**, 102002 (2003).

[17] V. V. Nesvizhevsky, A. K. Petukhov, H. G. Borner, T. A. Baranova, A. M. Gagarski, G. A. Petrov, K. V. Protasov, A. Y. Voronin, S. Baessler, H. Abele, A. Westphal, and L. Lucovac, Study of the neutron quantum states in the gravity field, Eur. Phys. J. C **40**, 479 (2005).

[18] G. Pignol, S. Ler, V. V. Nesvizhevsky, K. Protasov, D. Rebreyend, and A. Voronin, Gravitational resonance spectroscopy with an oscillating magnetic field gradient in the GRANIT flow through arrangement, Adv. High Energy Phys. **2014**, e628125 (2014).

[19] V. V. Nesvizhevsky and A. Yu. Voronin, *Surprising Quantum Bounces* (Imperial College Press, London, 2015).
[20] J. E. Lennard-Jones and A. F. Devonshire, The interaction of atoms and molecules with solid surfaces. III, Proc. R. Soc. London A **156**, 6 (1936).
[21] J. E. Lennard-Jones and A. F. Devonshire, The interaction of atoms and molecules with solid surfaces. IV, Proc. R. Soc. London A **156**, 29 (1936).
[22] M. V. Berry and K. E. Mount, Semiclassical approximations in wave mechanics, Rep. Prog. Phys. **35**, 315 (1972).
[23] I. A. Yu, J. M. Doyle, J. C. Sandberg, C. L. Cesar, D. Kleppner, and T. J. Greytak, Evidence for Universal Quantum Reflection of Hydrogen from Liquid He-4, Phys. Rev. Lett. **71**, 1589 (1993).
[24] J. J. Berkhout and J. T. M. Walraven, Scattering of hydrogen atoms from liquid-helium surfaces, Phys. Rev. B **47**, 8886 (1993).
[25] C. Carraro and M. W. Cole, Sticking coefficient at ultralow energy: Quantum reflection, Prog. Surf. Sci. **57**, 61 (1998).
[26] F. Shimizu, Specular Reflection of Very Slow Metastable Neon Atoms from a Solid Surface, Phys. Rev. Lett. **86**, 987 (2001).
[27] V. Druzhinina and M. DeKieviet, Experimental Observation of Quantum Reflection far from Threshold, Phys. Rev. Lett. **91**, 193202 (2003).
[28] T. A. Pasquini, Y. Shin, C. Sanner, M. Saba, A. Schirotzek, D. E. Pritchard, and W. Ketterle, Quantum Reflection from a Solid Surface at Normal Incidence, Phys. Rev. Lett. **93**, 223201 (2004).
[29] H. Friedrich and J. Trost, Working with WKB waves far from the semiclassical limit, Phys. Rep. **397**, 359 (2004).
[30] H. Oberst, Y. Tashiro, K. Shimizu, and F. Shimizu, Quantum reflection of He^* on silicon, Phys. Rev. A **71**, 052901 (2005).
[31] T. A. Pasquini, M. Saba, G.-B. Jo, Y. Shin, W. Ketterle, D. E. Pritchard, T. A. Savas, and N. Mulders, Low Velocity Quantum Reflection of Bose-Einstein Condensates, Phys. Rev. Lett. **97**, 093201 (2006).
[32] B. S. Zhao, S. A. Schulz, S. A. Meek, G. Meijer, and W. Schoellkopf, Quantum reflection of helium atom beams from a microstructured grating, Phys. Rev. A **78**, 010902(R) (2008).
[33] A. Yu Voronin and P. Froelich, Quantum reflection of ultracold antihydrogen from a solid surface, J. Phys. B **38**, L301 (2005).
[34] P. Froelich and A. Y. Voronin, Interaction of antihydrogen with ordinary atoms and solid surfaces, Hyperfine Interact. **213**, 115 (2012).
[35] G. Dufour, A. Gérardin, R. Guérout, A. Lambrecht, V. V. Nesvizhevsky, S. Reynaud, and A. Yu. Voronin, Quantum reflection of antihydrogen from the Casimir potential above matter slabs, Phys. Rev. A **87**, 012901 (2013).
[36] G. Dufour, Quantum reflection from the casimir-polder potential, Ph.D. thesis, Université Pierre et Marie Curie, 2015.
[37] A. Jurisch and H. Friedrich, Realistic model for a quantum reflection trap, Phys. Lett. A **349**, 230 (2006).
[38] J. Madronero and H. Friedrich, Influence of realistic atom wall potentials in quantum reflection traps, Phys. Rev. A **75**, 022902 (2007).
[39] P.-P. Crépin, E. A. Kupriyanova, R. Guérout, A. Lambrecht, V. V. Nesvizhevsky, S. Reynaud, S. Vasilyev, and A. Yu. Voronin, Quantum reflection of antihydrogen from a liquid helium film, Europhys. Lett. **119**, 33001 (2017).
[40] V. V. Nesvizhevsky, A. Yu. Voronin, R. Cubitt, and K. V. Protasov, Neutron whispering gallery, Nat. Phys. **6**, 114 (2009).
[41] P.-P. Crépin, G. Dufour, R. Guérout, A. Lambrecht, and S. Reynaud, Casimir-Polder shifts on quantum levitation states, Phys. Rev. A **95**, 032501 (2017).
[42] G. Dufour, P. Debu, A. Lambrecht, V. V. Nesvizhevsky, S. Reynaud, and A. Yu Voronin, Shaping the distribution of vertical velocities of antihydrogen in GBAR, Eur. Phys. J. C **74**, 2731 (2014).
[43] A. Yu. Voronin, V. V. Nesvizhevsky, G. Dufour, P. Debu, A. Lambrecht, S. Reynaud, O. D. Dalkarov, E. A. Kupriyanova, and P. Froelich, A spectroscopy approach to measure the gravitational mass of antihydrogen, Int. J. Mod. Phys.: Conf. Ser. **30**, 1460266 (2014).
[44] V. V. Nesvizhevsky, A. Voronin, P.-P. Crépin, and S. Reynaud, Interference of several gravitational quantum states of antihydrogen in GBAR experiment, Hyperfine Interact. **240** (2019).
[45] A. Y. Voronin, H. Abele, S. Baessler, V. V. Nesvizhevsky, A. K. Petukhov, K. V. Protasov, and A. Westphal, Quantum motion of a neutron in a waveguide in the gravitational field, Phys. Rev. D **73**, 044029 (2006).
[46] A. E. Meyerovich and V. V. Nesvizhevsky, Gravitational quantum states of neutrons in a rough waveguide, Phys. Rev. A **73**, 063616 (2006).
[47] R. Adhikari, Y. Cheng, A. E. Meyerovich, and V. V. Nesvizhevsky, Quantum size effect and biased diffusion of gravitationally bound neutrons in a rough waveguide, Phys. Rev. A **75**, 063613 (2007).
[48] M. Escobar, F. Lamy, A. E. Meyerovich, and V. V. Nesvizhevsky, Rough mirror as a quantum state selector: Analysis and design, Adv. High Energy Phys. **2014**, 764182 (2014).
[49] E. Wigner, On the quantum correction for thermodynamic equilibrium, Phys. Rev. **40**, 749 (1932).
[50] M. V. Berry, Semi-classical mechanics in phase space: A study of Wigner's function, Philos. Trans. R. Soc. London A **287**, 237 (1977).
[51] H. Cramér, *Mathematical Methods of Statistics, Princeton Landmarks in Mathematics PMS-9* (Princeton University Press, Princeton, NJ, 1946).
[52] P. Réfrégier, *Noise Theory and Application to Physics, Advanced Texts in Physics* (Springer, Berlin, 2004).